

The study of pinch regimes based on radiation-enhanced compression and anomalous resistivity phenomena and their effects on hard x-ray emission in a Mather type dense plasma focus device (SABALAN2)

D. Piriaei, T. D. Mahabadi, S. Javadi, M. Ghoranneviss, S. H. Saw, and S. Lee

Citation: *Physics of Plasmas* **22**, 123507 (2015); doi: 10.1063/1.4936801

View online: <http://dx.doi.org/10.1063/1.4936801>

View Table of Contents: <http://scitation.aip.org/content/aip/journal/pop/22/12?ver=pdfcov>

Published by the [AIP Publishing](#)

Articles you may be interested in

[Anomalous resistivity effect on multiple ion beam emission and hard x-ray generation in a Mather type plasma focus device](#)

Phys. Plasmas **18**, 103302 (2011); 10.1063/1.3647958

[Spatially resolved high-resolution x-ray spectroscopy of high-current plasma-focus discharges](#)

Rev. Sci. Instrum. **81**, 10E312 (2010); 10.1063/1.3483190

[Effect of anode shape on correlation of neutron emission with pinch energy for a 2.7 kJ Mather-type plasma focus device](#)

J. Appl. Phys. **106**, 023311 (2009); 10.1063/1.3177253

[Depleted uranium \(U 238 92 \) induced preionization for enhanced and reproducible x-ray emission from plasma focus](#)

Appl. Phys. Lett. **89**, 061503 (2006); 10.1063/1.2244055

[Comparative study of soft x-ray emission characteristics in a low energy dense plasma focus device](#)

J. Appl. Phys. **95**, 2975 (2004); 10.1063/1.1647269



PFEIFFER VACUUM

VACUUM SOLUTIONS FROM A SINGLE SOURCE

Pfeiffer Vacuum stands for innovative and custom vacuum solutions worldwide, technological perfection, competent advice and reliable service.

125 YEARS NOTHING IS BETTER

The study of pinch regimes based on radiation-enhanced compression and anomalous resistivity phenomena and their effects on hard x-ray emission in a Mather type dense plasma focus device (SABALAN2)

D. Piriaei,¹ T. D. Mahabadi,^{2,a)} S. Javadi,¹ M. Ghoranneviss,¹ S. H. Saw,^{3,4} and S. Lee^{3,4,5}

¹Plasma Physics Research Center, Science and Research Branch, Islamic Azad University, Tehran 1477893855, Iran

²Department of Physics and Biophysics, Tehran Medical Sciences Branch, Islamic Azad University, Tehran 1916893813, Iran

³INTI International University, Nilai 71800, Malaysia

⁴Institute for Plasma Focus Studies, 32 Oak Park Drive, Victoria 3148, Australia

⁵Universty of Malaya, Kuala Lumpur 50603, Malaysia

(Received 1 August 2015; accepted 16 November 2015; published online 9 December 2015)

In this study, by using argon and nitrogen as the filling gases in a Mather type dense plasma focus device at different values of pressure and charging voltage, two different kinds of pinch regimes were observed for each of the gases. The physics of the pinch regimes could be explained by using the two versions of the Lee's computational model which predicted each of the scenarios and clarified their differences between the two gases according to the radiation-enhanced compression and, additionally, predicted the pinch regimes through the anomalous resistivity effect during the pinch time. This was accomplished through the fitting process (simulation) on the current signal. Moreover, the characteristic amplitude and time scales of the anomalous resistances were obtained. The correlations between the features of the plasma current dip and the emitted hard x-ray pulses were observed. The starting time, intensity, duration, and the multiple or single feature of the emitted hard x-ray strongly correlated to the same respective features of the current dip. © 2015 AIP Publishing LLC. [<http://dx.doi.org/10.1063/1.4936801>]

INTRODUCTION

Dense plasma focus (DPF) devices, which are high voltage machines and belong to the class of Z-pinches, have always been attractive for producing short duration but high temperature and high density magnetized plasma. These devices can emit different kinds of high energy particles such as neutrons (when deuterium gas is used as the filling gas), electron and ion beams, and different kinds of radiations such as high intensity and short duration pulses of soft and hard x-rays.^{1–5}

One of the most interesting features of these machines is that they are cost-effective, versatile, and technically simple for construction comparing with the devices such as Z-pinch or Tokamak, especially in the field of nuclear fusion research and x-ray study. Since 5% and 10% of the stored capacitor energy are found to be converted into 1 keV x-rays for low and high energy DPF devices, respectively,^{6,7} an important part of the experimental research on x-ray emission from DPF devices has been oriented to the interesting applications such as contact microscopy, x-ray lithography, x-ray back-lighting, radiography, and micromachining.^{8–13}

The pinch phenomenon in plasma focus devices has significant role in hard x-rays production.¹⁴ Due to this fact, different kinds of pinch regimes can affect the quality, quantity, and features of the emitted hard x-ray. For this reason, finding the methods, which could predict each of these pinch

scenarios, would be desirable. In one approach, Lee *et al.*¹⁵ have considered the anomalous resistivity effect responsible for creating lengthy dip on the current trace during the pinch phase. Bernard *et al.*¹⁶ have given a good review on instability processes and also estimates anomalous resistance. In another attempt, Lee *et al.*¹⁷ have related the lengthy dip on the current trace during the pinch phase to radiation-coupled dynamics. It means that instead of considering a single system of a pinch followed by instability phases, it can be considered as successive pinches. Lee *et al.*^{18,19} and Beg *et al.*²⁰ have also shown that radiation-enhanced compression is much more likely to occur in higher-Z gases than in lesser-Z ones. Lee *et al.*,^{18,19} Oreshkin,²¹ Choi *et al.*²² and Haines²³ have discussed the radiation-enhanced compressions in pinches as varying degrees of radiative collapse from indefinite collapse (infinite density) to finite collapse, i.e., to a very narrow collapsed Z-pinch in which the pinch radius reaches a minimum size and does not become zero. In support of this idea, all of these researchers have stated that the pinch radius will approach zero until the contraction is terminated by additional mechanisms, such as re-absorption of the plasma radiation at high density, the onset of anomalous resistivity due to microinstabilities, the effect of finite voltage imposed by the external circuit, and the conversion of magnetic energy to ion thermal energy and pressure through viscous dissipation. Each of these mechanisms can prevent further radiative collapse and the reaching of zero pinch radius.

In the current research, the applicability and predictability of the Lee's computational model (including the two

^{a)}Author to whom correspondence should be addressed. Electronic mail: tadavari@gmail.com

versions (5-phase and 6-phase)),^{15,24,25} based on the two mentioned approaches above (radiation-coupled dynamics is incorporated in both of the two versions), have been tested. In this study, the experiments were carried out on a medium energy and high inductance Mather type DPF device (SABALAN2). Two different gases (argon and nitrogen) were used and the values of the pressure and the charging voltage varied which resulted in the occurrence of two different pinch regimes for each of the gases. These pinch scenarios could be explained by the model and their effects on the hard x-ray emission were investigated.

EXPERIMENTAL SETUP

In the present investigation, a medium energy (up to 25 kJ) Mather type DPF device (SABALAN2) was used, which was energized by a parallel set of fast discharging capacitors that could be charged up to 30 kV and provided the 62 μ F capacitor bank of the system. The schematic of the chamber, the electrodes (anode-cathode), the hard x-ray detector, and the appropriate circuit are shown in Fig. 1.

The electrode assembly possessed a central conventional cylindrical oxygen-free high conductivity copper rod as an anode (17 cm long and 4 cm diameter) which was surrounded symmetrically by 18 copper rods as the cathode array. Each cathode rod was 17.5 cm in length and 1 cm in diameter. The distance between the centers of the anode and the cathode array was 6.3 cm, i.e., the radius ratio of the cathode array to the anode was 3.15. The array of the cathode was screwed to a copper cathode base plate.

In order to facilitate the formation of the current sheath between the electrodes, a Pyrex glass insulator with a length of 4.5 cm and a thickness of 0.5 cm was used to separate the electrodes from each other. The electrode system was placed inside a stainless steel chamber and the chamber was vacuumed by a rotary vane pump. A hard x-ray detector was used to measure the hard x-ray radiation. This consisted of a photomultiplier tube coupled to a plastic scintillator.

A calibrated Rogowski coil together with an appropriate integrator was used to measure and record the current trace signal. All signals were recorded on a four-channel 100 MHz, 1 G-sample per second digital Tektronix oscilloscope.

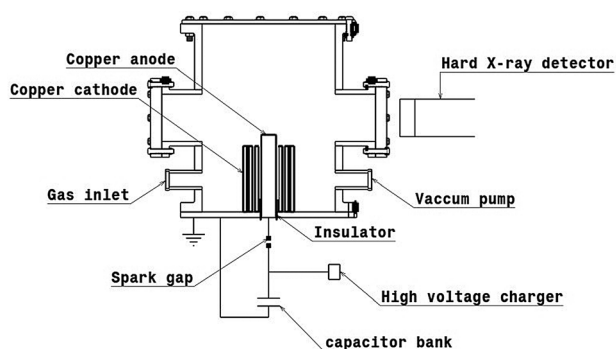


FIG. 1. Schematic of the DPF system (SABALAN2) which includes the anode-cathode assembly, its equivalent circuit, and the hard x-ray detector as the diagnostic of the device.

EXPERIMENTAL RESULTS

The experiments were carried out with nitrogen and argon as the filling gases in this device. For both of these gases, the pressure was altered within the range of 0.2–1 Torr, while the charging voltage was varied from 9 to 15 kV for each value of the pressure mentioned above. In all the experiments, the current and hard x-ray signals were recorded.

Two sets of the experiments were performed for the filling gases. In one set, the value of the operating pressure was kept constant, whereas the values of the charging voltage varied within its range and in another set the procedure was performed vice versa.

For each gas, two different kinds of pinch effect on the current trace signal were observed, which resulted in two different kinds of hard x-ray emission. In Figs. 2 and 3, it can be observed that the hard x-ray emission occurs simultaneously with the start of the current decrease or the current dip for the argon gas and in two sets of the experiments, a single pulse of the hard x-ray was observed. In Fig. 2, when the pinch effect was relatively weak with a first sharp current dip of 13 kA (a sharp narrow spike), a single narrow pulse of the hard x-ray was observed with FWHM of 60 ns and a broad base extending 450 ns; whereas in Fig. 3, a single broad pulse of the hard x-ray with FWHM of 160 ns and a broad base extending greater than 1.5 μ s appears at the same time as a strong pinch effect with a sharp current dip of 29 kA with slow recovery over a period greater than 1 μ s.

For the nitrogen gas, as shown in Fig. 4, the features of the pinch effect and the pulse of the hard x-ray were somehow similar to the one observed in Fig. 2 for argon gas, i.e., a relatively weak pinch effect with a sharp current drop (typically 12 kA in the form of a sharp narrow spike) is observed, and a single pulse of hard x-ray with FWHM of typically 50 ns appears simultaneously with the start of the pinch effect and the current dip. However, in Fig. 5, the pinch regime for the nitrogen gas was completely different from the one observed in Fig. 3 for argon gas. As depicted in Fig. 5, multiple narrow pulses of the hard x-ray (typically with FWHM values between 60 and 90 ns) appear simultaneously with the occurrence of the multiple dips in the current

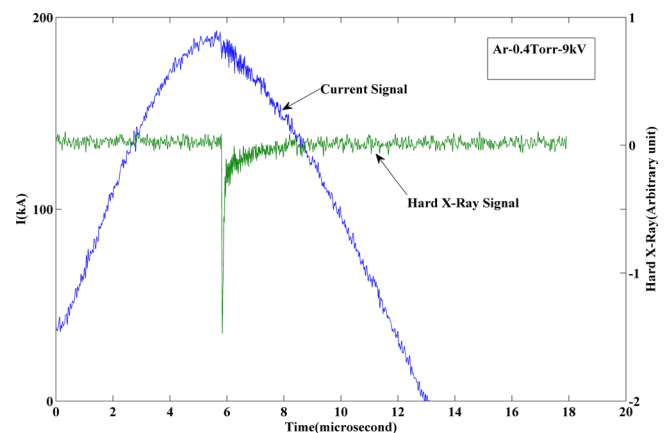


FIG. 2. The current trace and the hard x-ray signals of the argon gas at 0.4 Torr and 9 kV. The negative peak of the hard x-ray signal, which is narrow (FWHM of 60 ns), appears simultaneously with the current decrease. The first sharp part of the current dips is 13 kA and appears as a sharp spike.

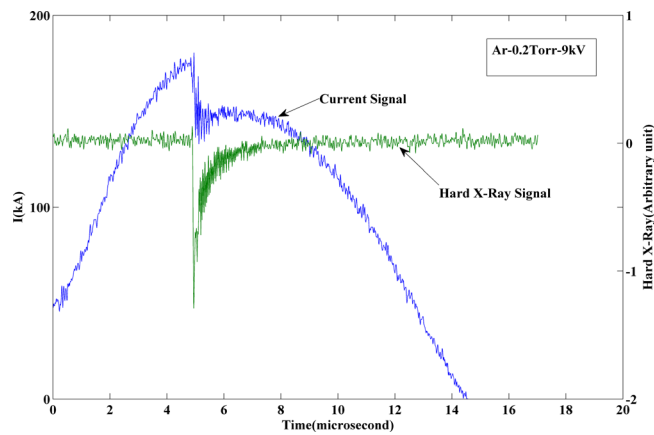


FIG. 3. The current trace and the hard x-ray signals of the argon gas at 0.2 Torr and 9 kV. The negative peak of the hard x-ray signal, which is relatively broad (FWHM of 160 ns with a broad base duration of greater than 1.5 μ s), appears simultaneously with the sharp current decrease (a sharp current drop of 29 kA) followed by a long period of current distortion of greater than 1 μ s.

trace signal (the current dips were narrow spikes typically between 20 and 29 kA in amplitude). The number of the hard x-ray pulses was the same as the number of the current dips. This feature was observed mostly for the nitrogen gas in two sets of the experiments when the value of the charging voltage was in the range of 12–15 kV.

DISCUSSION

The Lee's computational model²⁴ couples the electrical circuit with plasma focus dynamics, thermodynamics, and radiation, enabling a realistic simulation of all gross focus properties. In this model, the current trace signal is the fundamental indicator from which much important information, such as the axial and radial phase dynamics and the crucial energy transfer into the focus pinch, can be derived.

The exact time profile of the total current trace is governed by the bank parameters, by the focus tube geometry and the operational parameters. It also depends on the fraction of mass swept-up and the fraction of sheath current and the variation of these fractions through the axial and radial phases.

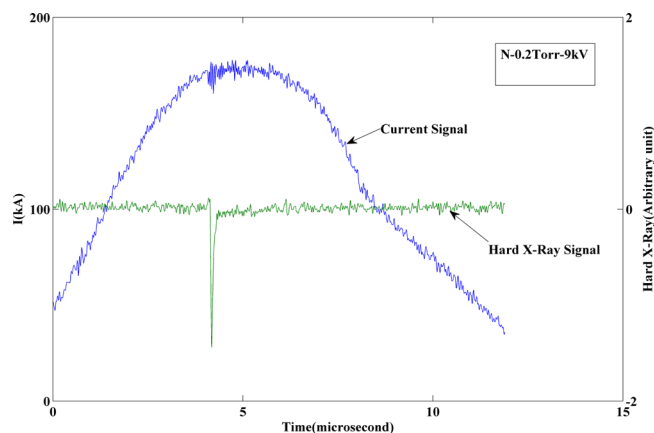


FIG. 4. The current trace and the hard x-ray signals of the nitrogen gas at 0.2 Torr and 9 kV. The single (negative) peak of the hard x-ray signal, which is narrow (FWHM of 50 ns), appears simultaneously with the sharp current decrease (appearing as a sharp negative spike).

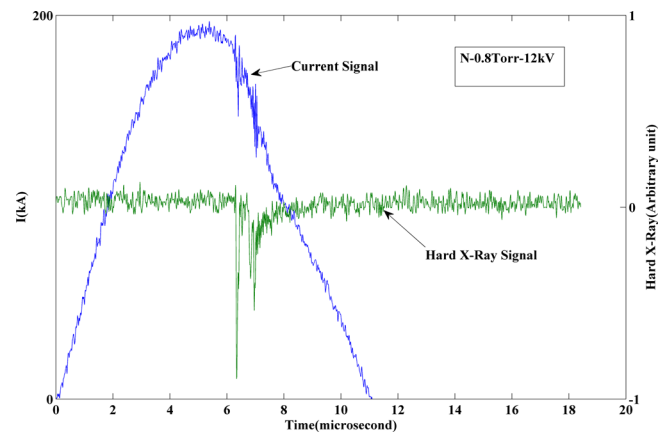


FIG. 5. The current trace and the hard x-ray signals of the nitrogen gas at 0.8 Torr and 12 kV. The negative peaks of the hard x-ray signal, which are narrow (typically FWHM between 60 and 90 ns), appear simultaneously with the sharp current dips typically between 20 and 29 kA in amplitudes and FWHM of between 150 and 350 ns.

These parameters determine the axial and radial dynamics, specifically the axial and radial speeds which in turn affect the profile and magnitudes of the discharge current.

Fig. 6 shows the fitting process for Fig. 2 in which the first version of the Lee's computational model (5-phase)²⁴ has been used and in which the fitting parameters for the argon gas at the pressure of 0.4 Torr and the charging voltage of 9 kV were $L_0 = 198$ nH, $C_0 = 64$ μ F, cathode radius $b = 6.3$ cm, anode radius $a = 2$ cm, anode length $z_0 = 17$ cm, stray resistance $r_0 = 7$ m Ω , axial mass factor $f_m = 0.027$, axial current factor $f_c = 0.7$, radial mass factor $f_{mr} = 0.035$, and radial current factor $f_{cr} = 0.7$.

There are two methods of interpreting data according to the two versions of the Lee's computational model.

In one method, during the pinch phase, different kinds of energy gain/losses relating to the Joule heating, bremsstrahlung, recombination, and line radiations occur. Their corresponding powers in a plasma column of radius a_{min} , length Z_{max} at temperature T are identified as¹⁹

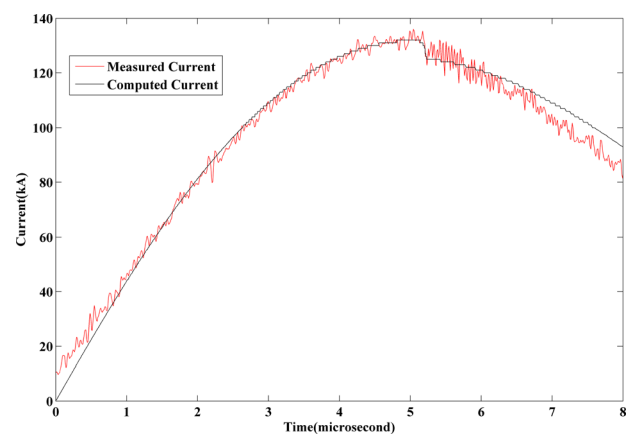


FIG. 6. The fitting process of the measured and the computed currents for the argon gas at 0.4 Torr and 9 kV according to the first version of the Lee's computational model (5-phase). Following the standard fitting procedure, the fitting is done only up to the end of the radial phase (i.e., the pinch), which is the bottom of the computed current dip; since the time region after the pinch is not important from the radiation point of view.

$$\frac{dQ_B}{dt} = -1.6 \times 10^{-40} N_i^2 Z_{eff}^3 (\pi a_{min}^2) z_{max} T^{0.5}, \quad (1)$$

$$\frac{dQ_{Rec}}{dt} = -5.92 \times 10^{-35} N_i^2 Z_{eff}^5 (\pi a_{min}^2) \frac{z_{max}}{T^{0.5}}, \quad (2)$$

$$\frac{dQ_L}{dt} = -4.6 \times 10^{-31} N_i^2 Z_{eff} Z_n^4 (\pi a_{min}^2) \frac{z_{max}}{T}, \quad (3)$$

$$\frac{dQ_J}{dt} = 1300 \cdot \frac{Z_{eff} \cdot z_{max}}{\pi a_{min}^2} \cdot I^2 \cdot T^{-\frac{3}{2}}, \quad (4)$$

where N_i is the number density, Z_{eff} is the effective charge number, Z_n is the atomic number of gas, a_{min} is the pinch radius, z_{max} is the pinch length, T is the plasma temperature, and I is the circuit current. The power terms are coupled to the dynamics of the current sheet in the code. Based on the information derived from the simulation, Fig. 7 shows the shares of these energy losses after the start of the radial phase and during the pinch time. For a better resolution, the time scale has been expanded; as shown in this figure, the loss of the energy in the form of Joule heating is more than the one related to the line radiation that causes radiation-enhanced compression,¹⁹ and the shares of the other two, i.e., energy losses relating to the bremsstrahlung and recombination radiations, are negligible. Therefore, in this scenario, the line radiation is not so significant to lead to noticeable radiation-enhanced compression. Without radiation-enhanced compression, the computed current dip has only a short dip which agrees with the dip's feature on the measured current in Fig. 2 for argon gas at 0.4 Torr and 9 kV.

Considering the other mechanism, it is assumed that the total energy transferred into plasma (EINP) is given by

$$EINP = \int_0^t I_p^2 \left(R_p + \frac{1}{2} \frac{dL_p}{dt} \right) dt, \quad (5)$$

in which I_p , R_p , and L_p are the plasma current, the plasma resistance, and the changing plasma tube inductance, respectively. The first and the second terms on the right side of Eq. (5) are the energies of the dynamic and the classical plasma resistances, respectively. The first term relates to the loss of the energy in the form of Joules heating which according to the simulation is small (0.24 J) and the second

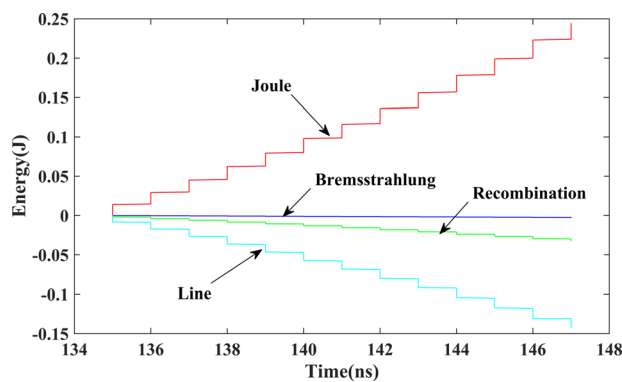


FIG. 7. Different components of energy losses for the case of Ar in Fig. 6 in the form of Joule heating, bremsstrahlung, recombination, and line radiations which occur only during the pinch time that are related to Fig. 2 and have been derived from the simulation according to the 5-phase code. The horizontal axis (time (ns)) has been expanded for a better resolution.

term which relates to the dissipation of the inductive energy is about 5% of the total transferred energy into the plasma during the pinch time. Therefore, both of these effects create a short dip on the computed current trace signal which again agrees with the dip's feature on the measured current in Fig. 2 for argon gas.

The 5-phase code²⁴ is not adequate for Fig. 3 because the simulated dip appeared much less than the measured one. Lee *et al.* solved this problem by including the effects of the anomalous resistances in a post-pinch phase in the extended 6-phase version of computational model.^{15,24,25} In this extended version, it has been assumed that after the pinch time, different kinds of instabilities and micro turbulences occur and all of these phenomena result in anomalous plasma resistance.¹⁵ This 6-phase model is found to be applicable to the PF devices whose $L_0 > 100$ nH and $L_0 \gg L_p$ which are the characteristics of the DPF devices used in this research with $L_0 \approx 202$ nH. As reported by Lee *et al.*,²⁶ at the end of the radial phase, the remnant energy stored in the plasma pinch is $\frac{1}{2} L_p I_{pinch}^2$, which is small compared with the remnant energy stored in the other inductances in the device which is $\frac{1}{2} (L_0 + L_a) I_{peak}^2$ in which L_a is the axial inductance. For machines with large L_0 , at the end of the dynamic pinch, a large amount of energy remains in the magnetic field. From their analysis, it appears that this large amount of remnant energy may then be consumed by the anomalous resistances. Fig. 8 shows the simulation results for Fig. 3 in which the 6-phase code^{15,24} has been used and in which the fitting parameters for the argon gas at the pressure of 0.2 Torr and the charging voltage of 9 kV were $L_0 = 202$ nH, $C_0 = 64$ μ F, cathode radius $b = 6.3$ cm, anode radius $a = 2$ cm, anode length $z_0 = 17$ cm, stray resistance $r_0 = 7$ m Ω , axial mass factor $f_m = 0.0265$, axial current factor $f_c = 0.7$, radial mass factor $f_{mr} = 0.45$, and radial current factor $f_{cr} = 0.7$. In this version, three anomalous resistances have been added sequentially to the post-pinch computation that each of them is given by

$$R = R_0 \left(e^{\frac{-t}{\tau}} - e^{\frac{-t}{\tau'}} \right). \quad (6)$$

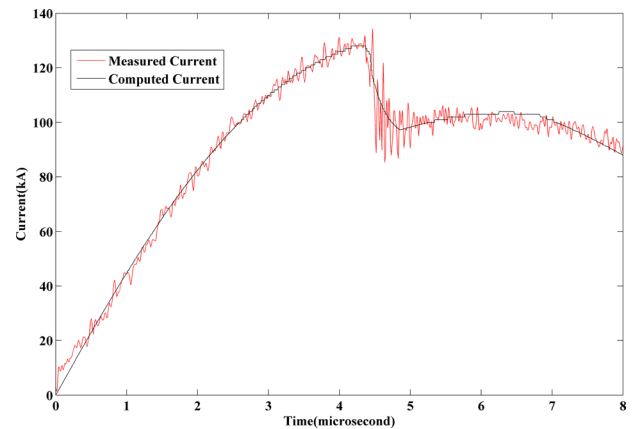


FIG. 8. The fitting process of the measured and the computed currents for argon gas at 0.2 Torr and 9 kV according to the second version of the Lee's computational model which shows a satisfactory agreement between the computed and the measured current traces by considering the anomalous resistivity effect.

TABLE I. Anomalous resistances used for the fitting of Fig. 8 in argon.

	R_0 (Ω)	t_1 (ns)	t_2 (ns)	End fraction time
Dip1	0.4	10	300	1.4
Dip2	0.01	10	500	1.3
Dip3	0.0001	10	150	1

In this equation, R_0 is a constant in the order of 1Ω ,^{15,16} t_1 is the characteristic rise time of the anomalous resistance, and t_2 is the characteristic fall time. Table I shows the features of the three anomalous resistances used in this fitting. In this table, the parameter of end fraction time shows the termination of each anomalous resistance and separates them from each other.

According to Table I, for argon at 0.2 Torr and 9 kV, this version of Lee's model typically estimates the magnitude of the primary (first) anomalous resistance of the post pinch plasma column of 0.4Ω with a rise time of 10 ns and a fall time of 300 ns.

As depicted in Fig. 8, there is good agreement between the computed and the measured current traces. The depths of the current dips of the two signals are nearly the same by fitting the three anomalous resistances sequentially following the procedures of the 6-phase code.

When we consider the case of argon at 0.2 Torr and 9 kV, the balance of Joule power and radiation power is significantly different when compared with that of argon at 0.4 Torr and 9 kV discussed earlier, shown in Fig. 9. The gain of energy from Joule heating is less than the loss of energy due to line radiation. Therefore, in this scenario, the line radiation is dominant and the strong radiative cooling reduces the energy, and the energy density of the pinched plasma and as a result causes the reduction of the plasma pressure. The compressing magnetic field is unaffected by the radiation, and the reduction in plasma pressure leads to additional compression. This mechanism may be considered as a radiation-enhanced compression. Therefore, the energy depletion is intense, which creates a lengthy dip on the computed current trace signal that again agrees with the dip's feature on the measured current in Fig. 8 for argon at 0.2 Torr.

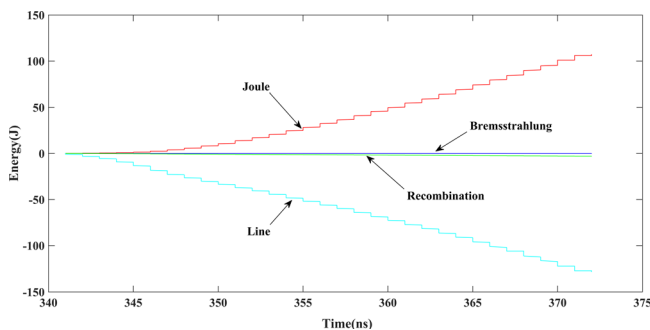


FIG. 9. Different components of energy losses for the case of Ar in Fig. 8 in the form of Joule heating, bremsstrahlung, recombination, and line radiations which occur only during the pinch time that are related to Fig. 3 and have been derived from the simulation according to the 6-phase code. The horizontal axis (time (ns)) has been expanded for a better resolution.

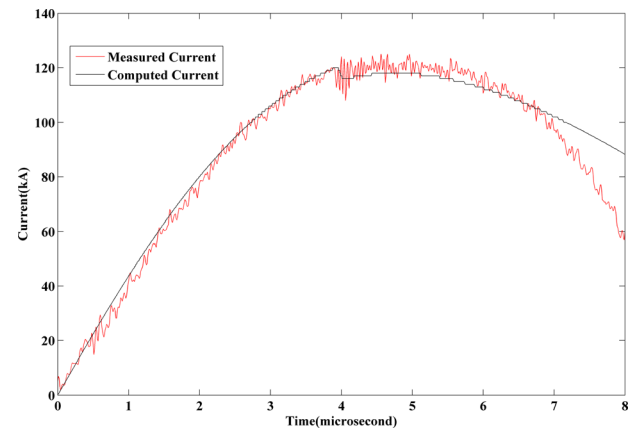


FIG. 10. The fitting process of the measured and the computed currents for nitrogen gas at 0.2 Torr and 9 kV according to the first version of the Lee's computational model (5-phase). Like Fig. 6, the fitting is done only up to the end of the radial phase (i.e., the pinch) which is the bottom of the computed current dip, since the time region after the pinch is not important from the radiation point of view.

The successful fitting process for the nitrogen gas at the pressure of 0.2 Torr and the charging voltage of 9 kV (Fig. 4), which has been shown in Fig. 10, reveals the similar trends as were described in Fig. 2 for the argon gas according to the two mechanisms. The fitting parameters (using the 5-phase code) in this figure were $L_0 = 198 \text{ nH}$, $C_0 = 64 \mu\text{F}$, cathode radius $b = 6.3 \text{ cm}$, anode radius $a = 2 \text{ cm}$, anode length $z_0 = 17 \text{ cm}$, stray resistance $r_0 = 7 \text{ m}\Omega$, axial mass factor $f_m = 0.03$, axial current factor $f_c = 0.7$, radial mass factor $f_{mr} = 0.05$, and radial current factor $f_{cr} = 0.7$.

Fig. 11 (same as Figs. 7 and 9) shows the energy losses for the nitrogen gas in Fig. 4. As depicted in this figure, the gain of energy from Joule heating is much more than radiation loss. Hence, there is no enhanced compression. The result is a short dip on the computed current trace that agrees with the one on the measured current trace in Fig. 10.

Similar to the fitting process done for argon gas in Fig. 3, successful fitting process was carried out for the nitrogen gas at the pressure of 0.8 Torr and the charging voltage of 12 kV (Fig. 5) according to the 6-phase code which includes the effect of anomalous resistances. The fitting parameters in this simulation were $L_0 = 202 \text{ nH}$, $C_0 = 64 \mu\text{F}$, cathode radius $b = 6.3 \text{ cm}$, anode radius $a = 2 \text{ cm}$, anode length $z_0 = 17 \text{ cm}$,

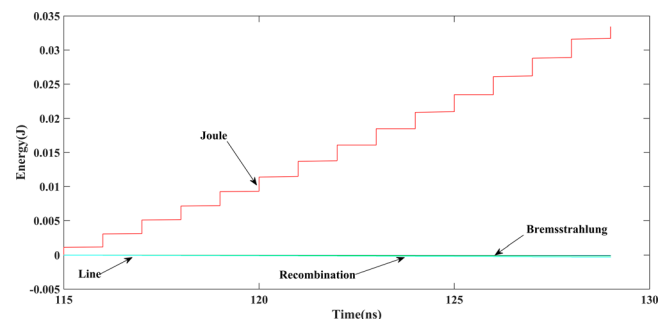


FIG. 11. Different components of energy losses for the case of N in Fig. 10 in the form of Joule heating, bremsstrahlung, recombination, and line radiations which occur only during the pinch time that are related to Fig. 4 and have been derived from the simulation according to the 5-phase code. The horizontal axis (time (ns)) has been expanded for a better resolution.

stray resistance $r_0 = 7 \text{ m}\Omega$, axial mass factor $f_m = 0.058$, axial current factor $f_c = 0.7$, radial mass factor $f_{mr} = 0.09$, and radial current factor $f_{cr} = 0.7$.

Three anomalous resistances have been added to the simulation, which have been considered according to the Table II. By considering these anomalous resistances, as shown in Fig. 12, both the total current depth and the multiple feature of the computed current signal match reasonably with the measured ones.

According to Table II, for nitrogen at 0.8 Torr and 12 kV, the second version of Lee's model typically estimates the magnitude of the primary (first) anomalous resistance of the post pinch plasma column of $0.4 \text{ }\Omega$ with a rise time of 10 ns and a fall time of 80 ns.

Fig. 13 for nitrogen (same as Figs. 7, 9, and 11) shows the energy gain/losses. As shown in this figure, the gain of energy from Joule heating is the dominant phenomenon for nitrogen. Radiation losses are small, and there is no radiation-enhanced compression in nitrogen. In all these cases with nitrogen gas, energy depletion is rather weak and it is highly possible for the plasma column to have subsequent compressions. This can explain the multiple dip features of the measured current trace.

Behbahani *et al.*¹⁴ have reported that one of the basic instabilities responsible for the growth of the turbulences during the pinch time is the $m = 0$ instability which occurs at the end of the compression phase and is the major reason for the emission of hard x-ray and energetic ions in the range of MeV. When the plasma radius shrinks to its minimum size, the magnetic pressure increases, which indirectly drives different kinds of micro-instabilities such as Buneman and lower-hybrid.²⁷ The plasma resistance R_p is inversely proportional to the plasma column radius during the pinch phase and the plasma electrical conductivity σ . The mentioned instabilities decrease σ , and as a result the plasma resistance will increase. This will increase the energy transferred into the plasma (first term in Eq. (5)), and the corresponding resistance will be responsible for the appearance of the multiple dips on the computed and the measured current signals in Fig. 12.

As reported by Behbahani *et al.*,¹⁴ there is a correlation between the current trace dip and the hard x-ray emission which can be readily seen in Figs. 2–5 where the hard x-ray emission begins simultaneously with the start of the current dip during the pinch time. It means that the start, the intensity, the number of the pulses, and the duration of the emitted hard x-ray depend strongly on the start, the depth (magnitude), the number, and the duration of the current dips.

Different kinds of simulations done on argon and nitrogen gases by considering the operational parameters in this research showed that the type of the pinch regime for the

TABLE II. Anomalous resistances used for the fitting of Fig. 12 in nitrogen.

	R_0 (Ω)	t_1 (ns)	t_2 (ns)	End fraction time
Dip1	0.4	10	80	0.9
Dip2	0.01	10	160	1.3
Dip3	0.3	10	250	4

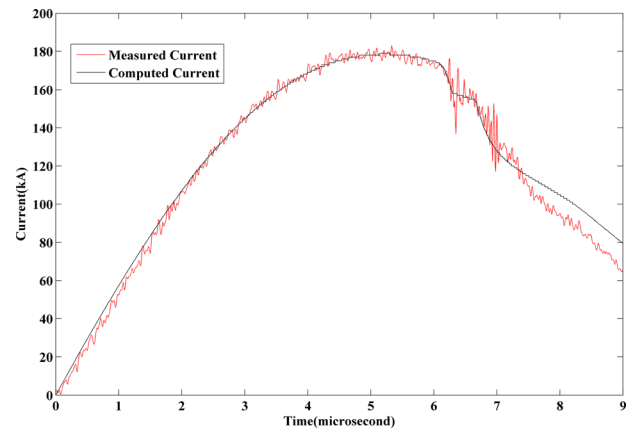


FIG. 12. The fitting process of the measured and the computed currents for nitrogen gas at 0.8 Torr and 12 kV according to the second version of the Lee's computational model which shows a satisfactory agreement between the computed and the measured current traces by considering the anomalous resistivity effect.

argon gas strongly depends on the fraction of mass swept-up during the radial phase, whereas the pinch scenarios of nitrogen gas were less sensitive to this parameter.

The pinch scenarios of Figs. 2 and 3 for argon gas can be explained in this way that the radial mass factor changes from shot to shot. When this parameter hits the correct value or more precisely, whenever the pressure factor (radial mass factor multiplied by pressure) is within a range of values (as computed from the code, for this machine at 9 kV with present configuration, this relevant pressure factor is around 0.04 to 0.2), the radiation is so intense that it cools the plasma in the pinch, lowering its static pressure; but the magnetic pressure is not affected by the radiation and continues to squeeze on the pinched plasma which now because of its radiation-reduced static pressure is squeezed further, until the plasma is dense enough for plasma self-absorption to stop further radiation. When such radiation-enhanced compression occurs in argon (as Fig. 9 depicts the dominant role of the line radiation), the enhanced compression pumps extra energy into the pinch, and after the compression, the magnetic field is relatively depleted of energy with little likelihood of further compressions. As shown in Fig. 3, there is typically only one huge current dip in argon operated in this regime. Whenever the pressure factor is not within the values

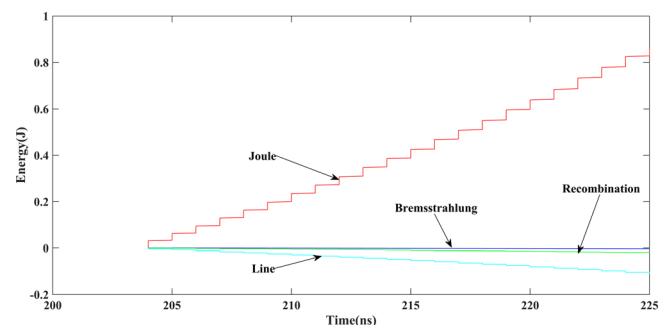


FIG. 13. Different components of energy losses for the case of N in Fig. 12 in the form of Joule heating, bremsstrahlung, recombination, and line radiations which occur only during the pinch time that are related to Fig. 5 and have been derived from the simulation according to the 6-phase code. The horizontal axis (time (ns)) has been expanded for a better resolution.

for dominant radiation, radiation-enhanced compression does not take place (as shown in Fig. 7, the line radiation is smaller than the Joule heating for this case of argon at 0.4 Torr) and the current dip will be short which is the case in Fig. 2.

There are indeed some differences between the pinch regimes of argon and nitrogen. These differences are related to the fact that the amount of line radiation from a plasma is proportional to Z_n^4 , Z_n being the atomic number of the gas or plasma (Eq. (3)). Due to the smaller $Z_n = 7$ for nitrogen, the amount of its line radiation is much less (1/44) compared with that of a typical argon pinch with $Z_n = 18$. Indeed, for all our operating range, there is no possibility of enough radiative cooling to cause enhanced compression in nitrogen plasma (as shown in Figs. 11 and 13). Therefore, pinch compression in nitrogen is typically less intense than argon like the one in Fig. 4. Whenever a pinch occurs near the peak current for nitrogen, after a compression, the energy depletion is relatively not so severe as the one in argon, and the current dip is small. This means that the current is still high and there is still a lot of magnetic energy left to drive further plasma processes including subsequent compressions. This is particularly the case for the plasma focus devices with large L_0 (like the one used in this research). Hence, a lot of energy stored in L_0 and in the pinch inductance is ready to be released into the pinch again in the form of one or more additional fast compressions (Fig. 5) in the case of nitrogen.

CONCLUSION

In this research, carried out on a Mather type DPF devices (SABALAN2), two different pinch regimes were observed in argon and nitrogen gases whose pressure and charging voltages were changed. The pinch regimes were explained according to the two mechanisms incorporated into the Lee 6-phase code: the radiation-enhanced compression and the anomalous resistivity effect.

Radiation-enhanced compression occurs whenever pinch radiation losses significantly exceed plasma energy gained from Joule heating. In our range of operation, radiation-enhanced compression typically occurs in argon at 0.2 Torr but not at 0.4 Torr. In nitrogen, radiation-enhanced compression does not occur over the whole range of pressures, due to its much lower atomic number. Thus, at 0.2 Torr, argon has a much deeper and longer current dip. This deep and long current dip leaves little remnant magnetic energy and thus argon tends to have only a single large current dip. On the other hand, nitrogen typically have smaller and multiple dips.

The 5-phase code could not fit fully the pinch regime current dip especially for the lengthy or multiple dips. The 6-phase code solved the problem by including the non-classical plasma or anomalous resistances. In this way, the magnitudes of the anomalous resistances of the post-pinch plasma and their time scales were obtained from fitting the post-pinch part of the current trace (Tables I and II). In both argon and nitrogen, the magnitude of the anomalous

resistance is measured as 0.4Ω with rise time of 10 ns. The fall times of the anomalous resistance in nitrogen is characterised as 80 ns whilst in argon it is 300 ns. Since there has not been much published data on the measurement of the anomalous resistances of the plasma focus pinch and post-pinch, this method is a useful diagnostic for measuring and extracting information on the gross anomalous resistance of the pinch.

Using the fitting procedure on the current trace signal, a good agreement was reached between the measured and the computed currents according to the experimental conditions for each gas. For each pinch regime, correlations were found between the starting time, intensity, duration, and the single or multiple features of the emitted hard x-ray and corresponding features of the current dips in the current signals.

- ¹M. Krishnan, *IEEE Trans. Plasma Sci.* **40**(12), 3189 (2012).
- ²S. Ahmad, S. S. Hussain, M. Sadiq, M. Shafiq, A. Waheed, and M. Zakaullah, *Plasma Phys. Controlled Fusion* **48**, 745 (2006).
- ³S. Hussain, S. Ahmad, M. Sharif, M. Sadiq, A. Waheed, and M. Zakaullah, *Phys. Lett. A* **349**, 236 (2006).
- ⁴A. Patran, L. C. Tan, D. Stoiculescu, M. S. Rafique, R. S. Rawat, S. V. Springham, T. L. Tan, P. Lee, M. Zakaullah, and S. Lee, *Plasma Sources Sci. Technol.* **14**, 549 (2005).
- ⁵M. Sadiq, S. Ahmad, A. Waheed, and M. Zakaullah, *Plasma Sources Sci. Technol.* **15**, 295 (2006).
- ⁶D. Wong, A. Patran, T. L. Tan, R. S. Rawat, and P. Lee, *IEEE Trans. Plasma Sci.* **32**, 2227 (2004).
- ⁷N. V. Filippov, T. I. Filippova, I. V. Khutoretskaia, V. V. Mialton, and V. P. Vinogradov, *Phys. Lett. A* **211**, 168 (1996).
- ⁸R. Lebert, W. Neff, and D. J. Rothweiler, *X-ray Sci. Technol.* **6**, 107 (1996).
- ⁹S. Hussain and M. Zakaullah, *Mod. Phys. Lett. B* **21**, 1643 (2007).
- ¹⁰S. Hussain, M. Shafiq, R. Ahmad, A. Waheed, and M. Zakaullah, *Plasma Sources Sci. Technol.* **14**, 61 (2005).
- ¹¹V. A. Gribkov, A. Srivastava, P. Lee, V. Kudryashov, and S. Lee, *IEEE Trans. Plasma Sci.* **30**, 1331 (2002).
- ¹²M. Sadiq, S. Ahmad, M. Shafiq, and M. Zakaullah, *Nucl. Instrum. Methods Phys. Res. B* **252**, 219 (2006).
- ¹³S. Lee, P. Lee, G. Zhang, X. Feng, V. A. Gribkov, M. Liu, A. Serban, and T. Wong, *IEEE Trans. Plasma Sci.* **26**, 1119 (1998).
- ¹⁴R. A. Behbahani and F. M. Aghamir, *Phys. Plasmas* **18**, 103302 (2011).
- ¹⁵S. Lee, S. H. Saw, A. E. Abdou, and H. Torreblanca, *J. Fusion Energy* **30**, 277 (2011).
- ¹⁶A. Bernard, H. Bruzzone, P. Choi, H. Chuaqui, V. Gribkov, J. Herrera, K. Hirana, A. Krejei, S. Lee, C. Luo, F. Mezzetti, M. Shadowski, H. Schmidt, K. Ware, C. S. Wong, and V. Zaita, *J. Moscow Phys. Soc.* **8**, 93 (1998).
- ¹⁷S. Lee, S. H. Saw, and J. Ali, *J. Fusion Energy* **32**, 42 (2013).
- ¹⁸S. Lee and S. H. Saw, *Phys. Plasmas* **20**, 062702 (2013).
- ¹⁹M. Akel and S. Lee, *J. Fusion Energy* **32**, 111 (2013).
- ²⁰F. N. Beg, I. Ross, A. Lorenz, J. F. Worley, A. E. Dangor, and M. G. Haines, *J. Appl. Phys.* **88**, 3225 (2000).
- ²¹V. I. Oreshkin, *Russian Phys. Journal* **40**(12), 1185 (1997).
- ²²P. Choi and C. D. Zaita, *AIP Conf. Proc.* **409**, 51 (1997).
- ²³M. G. Haines, *Plasma Phys. Controlled Fusion* **53**, 093001 (2011).
- ²⁴S. Lee, *J. Fusion Energy* **33**, 319 (2014).
- ²⁵See <http://www.plasmafocus.net>, <http://www.plasmafocus.net/IPFS/modelpackage/File1RADPF.htm>, <http://www.plasmafocus.net/IPFS/modelpackage/File2Theory.pdf>, and <http://www.plasmafocus.net/IPFS/modelpackage/UPF.htm> for Radiative Dense Plasma Focus Computation Package: RADPF (2010).
- ²⁶S. Lee and S. H. Saw, *Appl. Phys. Lett.* **92**, 021503 (2008).
- ²⁷M. Scholz, B. Bienkowska, I. Ivanova-Stanik, L. Karpinski, R. Miklaszewski, M. Paduch, W. Stepniewski, and K. Tomaszewski, *Czech. J. Phys.* **54**, 170 (2004).